Journal of Applied Geophysics 202 (2022) 104673

Contents lists available at ScienceDirect

Journal of Applied Geophysics

journal homepage: www.elsevier.com/locate/jappgeo

Imaging extensional fault systems using deep electrical resistivity tomography: A case study of the Baza fault, Betic Cordillera, Spain

Daniel Porras [a], Javier Carrasco [a], Pedro Carrasco [a], Pablo J. González [b,*]

[a] Dpto. Ingeniería Cartográfica y del Terreno. Geología, Escuela Politécnica Superior de Ávila, Universidad de Salamanca, Avd. Hornos Caleros nº 50, 05003 Ávila. Spain
[b] Department of Life and Earth Sciences, Instituto de Productos Naturales y Agrobiología (IPNA-CSIC), Av. Astrofísico Francisco Sánchez, 3, 38206 San Cristóbal de La Laguna, Santa Cruz de Tenerife, Spain

ARTICLE INFO

Keywords:
Normal faulting
Deep electrical resistivity tomography
Present-day tectonics
Baza Basin
Betics
Seismic hazard assessment

ABSTRACT

Seismic hazard assessment of present-day tectonic faults may be improved by studying their structure and kinematics. These features have been mainly determined by surface geological studies of exposed fault traces, structural lateral segmentation or paleoseismic trenches. All these approaches rely mainly on two-dimensional analyses of surface outcrops, while knowledge of the faults at depth remain largely inaccessible. To improve on such limitations, geophysical methods can be applied to establish detailed information on fault morphology and segmentation at depth. This work analyzes new results of a deep electrical resistivity tomography survey acquired across the Baza Fault, a present-day tectonic fault that controls the geometry of the Neogene intramountainous Baza Basin (Betic Cordillera, Spain). Interpretation of our preferred resistivity model reveals its detailed structure down to approximately 1000 m depth. The survey shows a minimum 2 km wide complex normal fault system, with rotational tilting blocks bounded by potentially listric normal faults. This study presents subsurface evidence of the Baza fault (F3), coincident the main topographic scarps. However, the geophysical model and geomorphic evidence also support a fault branch (F1) that might be an additional active seismogenic source. The geophysical survey technique presented in this study provides essential data to improve assessment of the seismogenic potential of the Baza Fault.

1. Introduction

There is strong evidence that the seismogenic potential of a fault depends, to a large degree, on its geometry (Wesnousky, 2008; Pace et al., 2016). In particular, its magnitude depends on the maximum spatial extent of the fault rupture propagation during seismic events. Therefore, better understanding of the geometry of a fault system is essential to understand seismogenic processes and, from a practical point of view, its future seismic potential (Scholz, 2019; Biasi and Wesnousky, 2017). Most relevant studies have made progress in characterizing their lateral segmentation and geometry, mainly due to easy access to surface expression of faults. However, the fault geometries at depth remain largely unknown. For instance, this lack of knowledge affects the estimated maximum rupture, which mainly relies on surface slip profiles and empirical fault-length relationships (Wells and Coppersmith, 1994).

The Baza Fault is one of the major active faults in the Betic Cordillera (Fig. 1). It presents background seismicity with low-magnitude events (Fig. 2), during the historical and instrumental record periods (IGN (Spanish Instituto Geográfico nacional) seismic Catalogue, 2020; Martínez-Solares and Mezcua, 2002). The largest historical earthquake (M_w 6.0) occurred in 1531 CE, known as the Baza earthquake, destroying Baza and Benamaurel towns (Sanz de Galdeano et al., 2012). The Baza fault kinematics indicate predominant normal faulting with a minor strike-slip component. Previous studies have established it as an active and potentially seismogenic fault source (Sanz de Galdeano et al., 2012; Medina-Cascales et al., 2020). However, those estimates are mainly based on its surface expression. Therefore, new work is necessary to constrain the fault geometry and segmentation, in particular at depth.

In this study, the data and models arising from a new geoelectrical survey are presented. The geoelectrical profile with 4.5 km-long was acquired across the Baza Fault in its south-western sector. The relatively large aperture of this survey allowed us to reach greater depths than usual, improving our knowledge of the deep (1000 m depth) fault structure and characteristics. Resistivity surveys have been widely applied in mining, geology, engineering and environmental studies to

* Corresponding author.
E-mail address: pabloj.gonzalez@csic.es (P.J. González).

https://doi.org/10.1016/j.jappgeo.2022.104673
Received 6 May 2021; Received in revised form 25 March 2022; Accepted 9 May 2022
Available online 12 May 2022

solve multiple problems, including structural and active seismic zones, and provide high-resolution subsurface resistivity models at shallow depths <200 m (Kolawole et al., 2018; Suzuki et al., 2000; Steeples, 2001), which is the usual length of cables used in industry. The deep electrical resistivity tomography (DERT) is a specific survey acquisition and modeling method that analyzes larger depth ranges, usually between 500 and 1500 m depth. These have been specifically applied in the study of structural and active seismic zones (Balasco et al., 2011; Günther et al., 2011; Pucci et al., 2016; Rizzo et al., 2004).

In this study, a 2D deep electrical resistivity tomography model was obtained applying a damped least squares inversion. Model selection was carried out using automatic methods, trading-off data misfit and model complexity. The preferred final model compared favourably against literature, geological-structural data and previously available geophysics. It allows for an improved, new and detailed geological and structural view of the Baza Fault at depth. The model suggests that the system is segmented with several normal faults. Some normal fault branches were not previously recognized and might not be currently active. However, an unmapped fault branch shows geomorphic evidence for recent Quaternary fault slip. The fault system features separate rotational tilting blocks, indicating a potential listric geometry at greater depths (>1000 m). The new results confirm and extend previous surveys establishing the fault geometry and kinematics using surface analysis, available geophysical data, gravity (Alfaro et al., 2008) and seismic methods (Haberland et al., 2017). Hence, our study contributes to the seismic hazard assessment, and generally to tectonosedimentary reconstruction of the Baza basin, e.g., basement throw estimation.

2. Geological setting

The Baza Fault is located in the Baza Basin, a sub-basin within the main Guadix-Baza Basin. The wider Guadix-Baza Basin is the largest intramontane Neogene basin in the Betic Cordillera (Vera, 1970a, 1970b). This Cordillera is an orogen resulting from a Neogene NNW – SSE oblique convergence of 3–5 mm/year between the Eurasian and Nubian plates (Nocquet, 2012; Palano et al., 2015). The shortening is synchronous with an ENE-WSW orogen-parallel extension (Galindo Zaldívar et al., 1999; Marín-Lechado et al., 2017). The regional ENE–WSW extension in the central Betics accomodates between 0.5 and 1.5 mm/yr (Palano et al., 2013). This tectonic extension rate is accommodated by NNW–SSE striking normal faults like Baza Fault (Galindo Zaldívar et al., 1989, 1999; Sanz de Galdeano et al., 2012; Sanz de Galdeano et al., 2020), further developing the basins (e.g., Baza basin).

The Baza Fault delimits the NNW-SSE border of the Baza Basin (Galindo Zaldívar et al., 1999). With more than 35 km of surface topographic expression, the Baza Fault is a normal fault system with a relatively acute curved trace. The fault system strikes from N-S at the northern end to a NW-SE trend at its middle-southern termination. Overall, it presents numerous parallel splays, increasing in number towards the southern end. The Baza Fault dips from 45° to 65° to the East (Alfaro et al., 2008; Sanz de Galdeano et al., 2012; Haberland et al., 2017), with an inferred vertical slip rate of 0.12–0.49 mm yr^{-1} calculated using the displaced glacis (ca. 500Kyr - García Tortosa et al., 2011; Sanz de Galdeano et al., 2012). The fault seems to have been active since the Late Miocene (García-García et al., 2006). The relatively fast fault slip rate of the Baza Fault generates a half-graben structure on its hanging wall, with a maximum sediment thickness of 2200 m based on

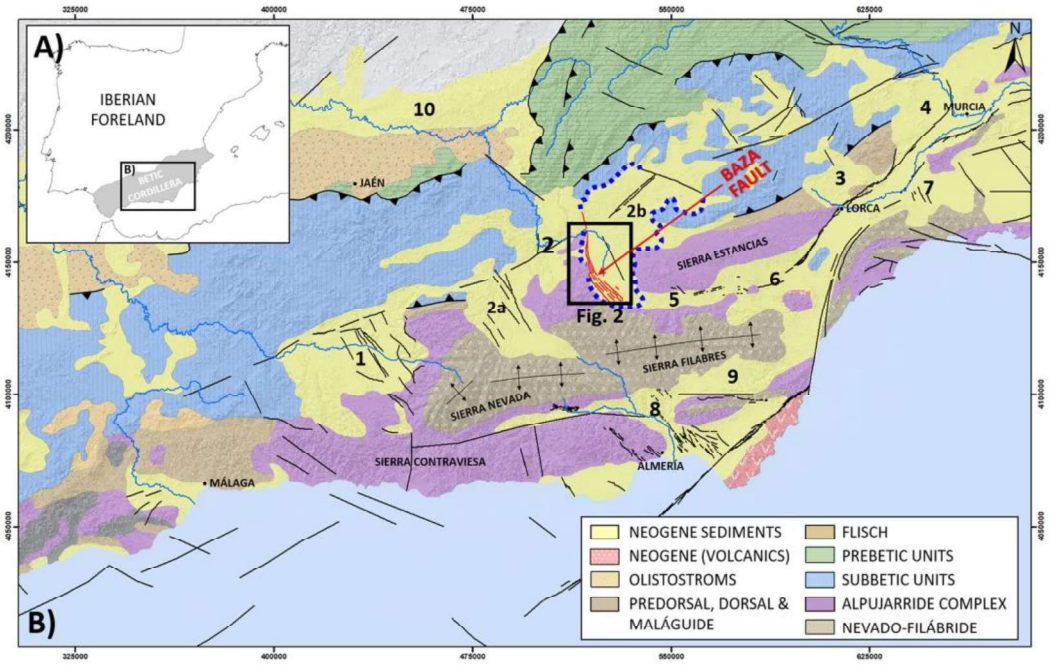

Fig. 1. A) Location of the Betic Cordillera. B) Simplified geological map of the Betic Cordillera. Numbers indicate intramontane sedimentary basins. 1: Granada basin; 2: Guadix-Baza Basin; 2a: Guadix subbasin; 2b: Baza subbasin; 3: Lorca basin; 4: Mula-Fortuna basin; 5: Almanzora corridor; 6: Huerca Overa basin; 7: Totana basin; 8: Tabernas basin; 9: Sorbas basin. Blue dotted line indicates the limits of the Baza subbasin, and black rectangle shows the Fig. 2 location. (For interpretation of the references to colour in this figure legend, the reader is referred to the web version of this article.)

seismic surveys (Haberland et al., 2017). The basin was filled by sediments over Triassic metamorphic basement rocks from the Alpujarride Complex (García-Dueñas et al., 1992; Orozco and Alonso-Chaves, 2002). Baza Basin infills consist of Upper Miocene marine deposits, which transition upwards into continental deposits during the Pliocene / Pleistocene age. The progressive uplift disconnecting the basin from the Mediterranean Sea was caused by this transition (Vera, 1970a, 1970b; Soria et al., 1998; Rodríguez-Fernandez et al., 2012). Later on, the higher subsidence of the hanging wall of the Baza Fault generated an endorheic fluvial and lacustrine system until the late Pleistocene, through capture of its drainage system by the Guadalquivir fluvial network (Sanz de Galdeano and Vera, 2007; Sanz de Galdeano et al., 2012; Alfaro et al., 2008). The Quaternary sedimentation is restricted to depressed areas, forming alluvial fans and piedmont systems, which are affected frequently by the Baza Fault slip, generating stepped fault scarps (García Tortosa et al., 2008; García Tortosa et al., 2011; Castro et al., 2018).

2.1. Previous geophysical studies

The Baza basin structure and its *syn*-tectonic infilling sedimentation have been extensively studied at regional scale (basin-wide). However, there is scarce information about the detailed subsurface structure of the basin near the Baza Fault. Previous studies were mainly based on the use of surface geological and geomorphological data (Sanz de Galdeano and Vera, 1992; Soria et al., 1998; Rodríguez-Fernandez et al., 2012). Recent work further suggests a tectono-stratigraphic evolution from 6 Ma to 0.6 Ma, marked by a long sedimentary history. The Baza fault induced more than 1000 m of subsidence, supported by geological evidence and migrated P-receiver functions that indicate variable crustal thicknesses under the hanging wall and footwall of the Baza fault (Pérez-Peña et al., 2018).

Alfaro et al. (2008) carried out a gravimetric study, recording negative anomalies. Those anomalies are the maximum negative values found in the entire Betic Cordillera. The gravity anomaly map shows two gravity minima along the Basin axis running parallel along the fault strike: one south of the village of Benamaurel, and a secondary one at the southeast of Baza town. The inferred basin structure in this study estimated a 2000–3000 m throw in the basement, with the southern section formed by a structurally simple half-graben and the northern area significantly more complex, with various fractures compartmentalizing the basement.

In 1977, a seismic reflection line was shot crossing the Baza fault and the western part of the basin (BT-2 seismic line, ITGE, 1999). This line struck NNW-SSE, and obliquely crossed the Baza fault. The survey results were not favorable enough to illuminate the fault zone or the basin's structure, due to its orientation with respect to the Baza fault strike. However, it revealed tectonic complexity with some associated synthetic and antithetic faults. The BT-2 seismic line showed the contact between the acoustic basement and the sedimentary basin infill, with the alternation of strong reflectors and transparent levels. In addition, the ESCI-Béticas project contained two deep-seismic profiles in the Baza Basin (García-Dueñas et al., 1994; Jabaloy et al., 1995). Due to the focus on imaging the complete crust structure, this survey did not show detailed structural information on the basin (Jabaloy et al., 1995). Only a small reflectivity layer in the upper part (0–2 s) confirmed the asymmetric shape of the basin sediments and the inferred active western boundary fault, the Baza fault. Finally, Haberland et al. (2017) shot three high-

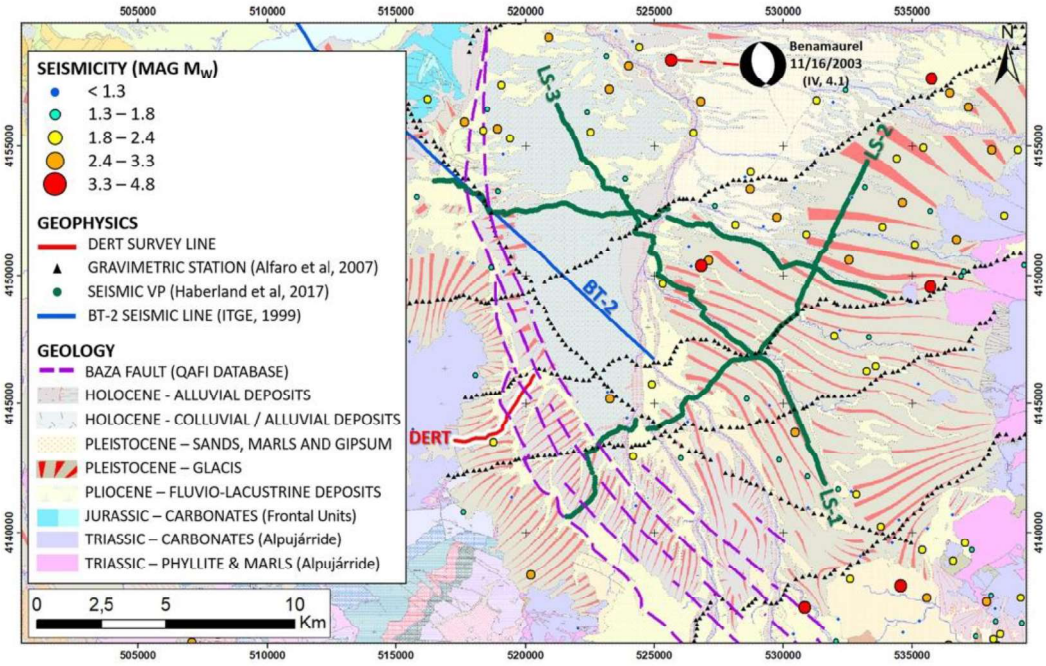

Fig. 2. Geological map of the southern part of the Baza Basin. Deep electrical resistivity tomography survey line is displayed (red line) with the Baza Fault trace with its different splays (Quaternary Faults Database of Iberia (QAFI)), previous geophysical surveys (gravimetric and seismic), and seismicity, including the 4.1 Benamaurel earthquake focal mechanism (Instituto Andaluz de Geofísica, https://iagpds.ugr.es/). (For interpretation of the references to colour in this figure legend, the reader is referred to the web version of this article.)

resolution deep-seismic profile lines across the basin and fault in different directions. The study revealed and confirmed the asymmetric shape of the infilling sediments. It detected the continuance at depth of the Baza fault and several others throughout the basin, affecting the deeper sedimentary layers. The seismic study also constrained the maximum sediment thickness to 2200 m.

2.2. Seismicity of the Baza fault

The Baza Fault is one of the most active faults in the central Betic Cordillera, presenting a general low-magnitude seismicity during the historical and instrumental record (Spanish Instituto Geográfico Nacional (IGN) catalogue; Martínez-Solares and Mezcua, 2002), with an important maximum historical earthquake in 1531 (VIII-IX) (Martínez-Solares and Mezcua, 2002). This event is known as the Baza earthquake, and was estimated at a magnitude of M_w 6.0. This earthquake destroyed the original settlements of Baza and Benamaurel (Sanz de Galdeano et al., 2012). There is also geological evidence of previous large events, with the presence of seismites or liquefaction features, and earthquake-induced landslides (Alfaro et al., 1997; Gibert et al., 2005).

The seismogenic potential of the Baza Fault was preliminarily estimated by Sanz de Galdeano et al. (2012) to be of the order of M_w 6.9 (Wells and Coppersmith, 1994). More recent estimates for M_{max}, to predict if a future seismic event would rupture the entire Baza fault, range from Mw 6.2 to Mw 7.1 using different empirical laws, and highlight the considerable uncertainties involved (Medina-Cascales et al., 2020).

3. Data and methodology

3.1. Electrical resistivity tomography for fault detection

Electrical Resistivity Tomography (ERT) is a widely used geophysical technique. Among many applications, it has been successfully applied to image subsurface structures and, in particular, faults (Suzuki et al., 2000; Steeples, 2001; Caputo et al., 2003; Kolawole et al., 2018). The ERT method is based on taking measurements of ground resistivity along a connected line or array, by applying an electric current to the subsurface via two metal stakes (*current electrodes*) coupled to the ground. The current passing through the ground sets up an electrical potential in the subsurface. The difference in electrical potential between two additional *potential electrodes* is measured as a voltage. Using Ohm's law, this voltage can be converted to values of apparent resistivity for the ground between the two potential electrodes. Measurements are repeated, rolling over in sets of four electrodes. To reach greater depths, four electrodes with a wider spacing are selected, usually a multiple of the first set. This is repeated with wider separations, in this way increasing the effective depth of the survey. A subsurface ground-resistivity image or pseudo-section is generated using the input current, measured voltage and the array geometry (Edwards, 1977). Hence, the array geometry varies and determines the survey sensitivity, with its two main parameters being the array spacing and aperture. The separation between electrodes controls the spatial resolution, while the depth penetration depends strongly on the total distance spanned by the electrode array.

Fault detection is based on resistivity contrasts in the subsoil between the geological units, which provide information on the physical conditions of the rocks (Caputo et al., 2003; Drahor and Berge, 2017; Storz et al., 2000). Despite its usefulness, the geoelectrical method to investigate the Baza Fault system has not applied in previous studies. Here, a modification of the deep ERT (DERT) is applied, aiming to reach greater depths. DERT has been applied to study deep structures including faults and active seismic zones (Balasco et al., 2011; Günther et al., 2011; Pucci et al., 2016; Rizzo et al., 2004), the shape of basins and infilling materials geometry and characteristics (Rizzo et al., 2019; Rizzo and Giamapolo, 2019), and also, geothermal systems (Carrier et al., 2019; Troiano et al., 2019).

3.2. Survey and data acquisition

During the study, ERT data were collected over a line with 4.5 km length. The array was set up across the southern sector of the Baza Fault. In that region, the fault system strikes NW–SE, and it is composed of several splays with a local width of about 2.5 km (Fig. 2). The line was acquired using a roll-along acquisition technique dividing the total line length into two segments. Segments were deployed using two 3 km lengths of multicore reversible cable with electrode separation of 100 m. A Syscal Pro resistivity meter was used, with a 1200 W AC/DC converter. The recording array selected was Pole-Dipole, deploying an infinite electrode orthogonal to the line direction with a minimum offset of 5 km, designed with a 100 m X spacing and n values from 1 to 29, with a total 435 data points (Fig. 3-1). This array configuration was selected to obtain high penetration capability, strong signal and high-density data (Carrasco García, 2013). A 50% segment length overlap was used to avoid loss of information at depth (Fig. 3-2). The inversion was based on a model of 364 blocks distributed in 11 model layers, where the minimum pseudodepth was 51.9 m and maximum 899.4 m.

Data quality in ERT during acquisition depends on three factors, resistivity of the materials, noise, and contact resistance. The first two factors are mitigated by using a high-power transmitter and an AC/DC converter, incrementing the effective working voltage. The third factor impact depends on the resistivity of the most superficial layer of the terrain. In case of not allowed contact resistances, over 2000 Ohm for conductive and 20,000 Ohm in resistive materials (heuristic criteria) longer and/or multiple linked electrodes are installed at the electrode position, and if needed, enhancing the galvanic contact of the electrodes with the ground can be enhanced by adding salt water solution. Electrode locations were determined using a handheld GPS with a horizontal accuracy ≈3 m. Topography heights were extracted for the GPS coordinates and a 5 m resolution DEM (Instituto Geográfico Nacional, https://centrodedescargas.cnig.es/CentroDescargas/index.jsp). The elevation values of each data point were used during the data inversion.

3.3. Inverse modeling strategy

The following data processing approach was applied. The field raw data (binary) into ASCII format to numerically process the field datasets were converted. Using X2IPI software, outlier data points were removed following criteria that there were un-measured intensities or that measurement was less than 100 mA (Robain and Bobachev, 2002). Then, the two roll-along survey segments were combined into a single 2D data file. Topographic data were assigned to each node. Finally, the apparent resistivity data were inverted via using a linearized least-squares algorithm to obtain true resistivity models (Loke and Dahlin, 2002). The ERT data was modeled using the commercial RES2DINV software (Loke and Barker, 1995). This code utilizes a finite element or a difference algorithm to obtain the forward modeling of the voltage response to current injection. The resistivity models produced by RES2DINV are divided into a number of rectangular blocks with specific resistivity values derived from the field measurements. Apparent resistivity data is finally presented as a pseudo-section, a contour diagram in which apparent resistivity values are assigned depending on the array type, to a predefined location (Telford et al., 1990).

The inversion method selected was the smooth L2 norm or smoothness-constrained least-squares optimization method, depending on a damping factor. The L2 norm is supposed to minimize the sum of squares between the observed and calculated apparent resistivity values, generating smooth variations in resistivity within the inversion model. The inversion process starts from the initial model parameters and damping factors, which are refined by an iterative process (Lines and Treitel, 1984). The discrepancy between the calculated values of apparent resistivity and those inferred from field data are expressed

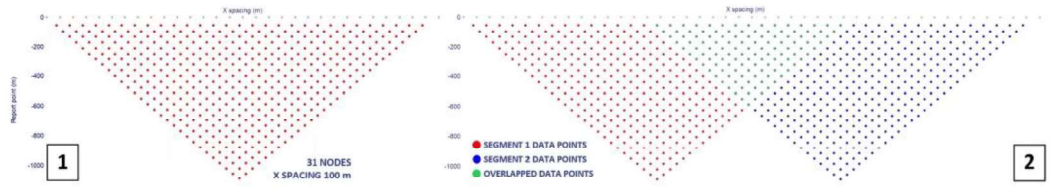

Fig. 3. 1) Sketches of the designed acquisition array configuration, the array consisted of 31 nodes with 100 m spacing and $n = 1$ to 29. 2) Sketch of data points distribution, highlighting the 50% recording segment length overlap.

through the root mean square (RMS).

The model results depend on the damping factor and number of iterations. Therefore, the effect of the number of iterations was evaluated for this investigation (Fig. 4). The effect was analyzed by running different inversions while varying the number of iterations, a procedure known as convergence curve method. The curve displays how the RMS misfit error varies with the number of iterations. As shown in Fig. 4-a, the curve shows an RMS value of 42.09% for the first iteration and a final RMS value of 22.75% after 10 iterations. The RMS misfit between the observed and computed data (RMS) rapidly decreases before the 3rd iteration and stabilizes with a minor decrease after the 6th iteration. This indicates that to obtain stable model results with our discretization and dataset the number of iterations should be between 3 and 6.

The effect of the starting range of damping factors was also tested. The optimal damping factor is found iteratively but can be affected by the initial values. RES2DINV allows selection of an initial and minimum pair of damping factors, as initial values. Therefore, 10 experiments were conducted (Fig. 4 b) and different sets of initial and minimum damping factors, following by a one-fifth rule to establish the minimum were provided (Loke, 2019, Geotomo Software). As already shown, the number of iterations rapidly reduces the RMS of the data misfit. The curves obtained show that there are no significant variations in the inversion results based into the initial damping factor variations, indicating that the software inversion routine obtains an optimum smoothing automatically, with little necessity of fine-tuning (Fig. 4-b). According to this analysis, subsequent models were obtained fixing the initial and minimum damping factors as 0.4 and 0.08 respectively.

4. Inversion results

According to the choice of inversion parameters from the previous section, two geoelectric models representing smoother and rougher possible solution were selected for further discussion (Fig. 5). Model A represents an example of a smooth model and higher misfit value, while Model B is our preferred model (parsimonious model). Model B is preferred because it is the smoothest model that achieves the lowest RMS value in the lowest number of iterations. Increasing the number of iterations do not further improve misfit levels. Models with higher model iterations do not achieve lower RMS values (Fig. 4A). Model A was obtained at iteration 3, and shows an RMS of 28.79% (Fig. 5-1). This model shows great variability in resistivity values, ranging from 20 up to more than 3000 Ohm•m. The main characteristic of the model is the presence of two resistive bodies (A and B), and two conductive zones (C and D). The two resistive bodies ($\rho > 1500$ Ohm•m) are located in the western part of the profile, outcropping (A), and in the central section along the model's deeper sections (B). The anomalies lack strong resistivity gradient transitions (> 500 Ohm•m/100 m) in resistivity values to the conductive zones. However, the eastern half of the profile is dominated by conductive materials (D) ($\rho < 400$ Ohm•m), although these materials are overlaid by subhorizontal anomalies with higher resistivity values (E). There is also a conductive body (C) present in the deeper parts, located to the SW of the modeled profile. Between the 800 and 1600 m profile length marks, the model shows greater variability in resistivity at shallow depths, forming a region with increased heterogeneity of resistive and conductive anomalies (F).

Model B was obtained after iteration 6, and shows an RMS of 23.1% (Fig. 5-2). It presents some notable variations with respect to model A.

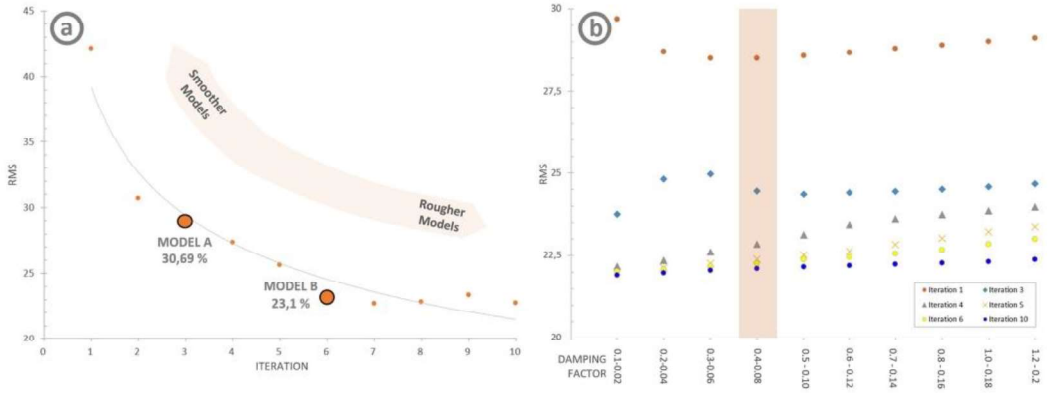

Fig. 4. a) RMS misfit variation as a function of the number of iterations to search for the optimal damping factor; b) Results of the automatic search for the regularized least squares inversion. Increasing the number of iterations decreases the RMS of the models rapidly but this flattens after a third iteration. In addition, the starting damping factor does not strongly affect the final misfit of the inverted models.

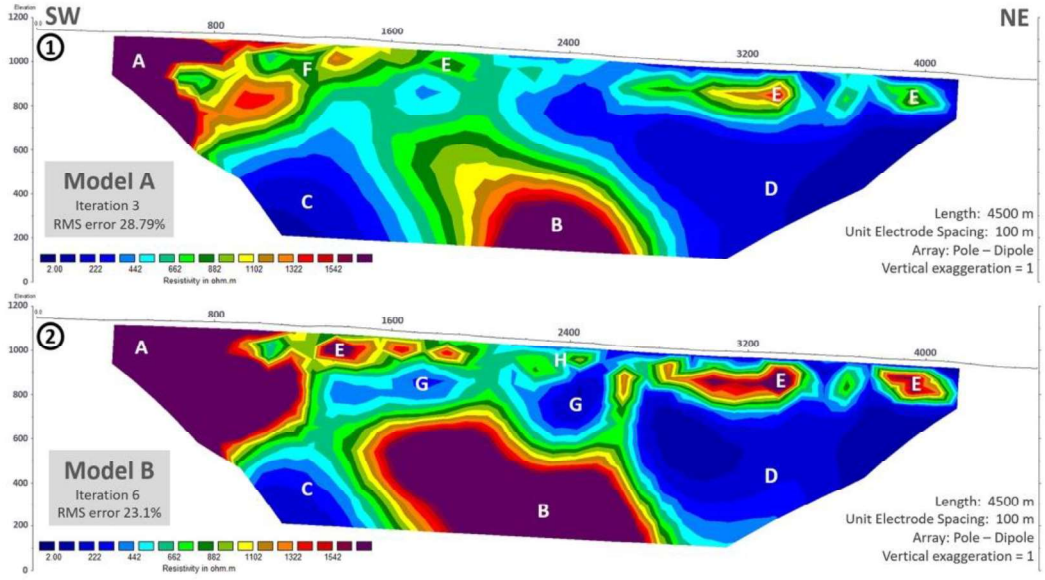

Fig. 5. (1) Model A (Iteration 3, RMS error 28.79%), (2) Model B (Iteration 6, RMS error 23.1%). A to G: resistive and conductive bodies delimited in the models.

The size and morphology of the resistive bodies (A and B) are larger and shows a higher resistivity gradient (> 500 Ohm•m/100 m) to the conductive zones than in model A, permitting the resistivity contrast limits of the anomalies to be established more precisely. The central resistive body (B) shows subvertical edges on its eastern and western sides. Resistive body B also presents a clear subvertical step discontinuity in its central part. Above the central discontinuity, a much clearer upper conductive area (G) is perceptible, which appears to be separate from some upper outcropping resistive layers (E and H). This horizontal outcropping resistivity layer shows a more continuous extent and can be differentiated into two types, in terms of resistivity value: E (more resistive) and H (less resistive). Comparing the main conductive zones, the conductive zone (C) in the southwest part of the model covers a smaller area than in model A.

5. Discussion

5.1. Model selection and validation

Geophysical inversion is inherently ill-posed and an infinite number of solutions are consistent with the observational data. Therefore, regularization is necessary to reduce the model space. Nevertheless, there still remains a variety of geologically acceptable models. Here, the results with external datasets to further reduce the model space are combined. The aim is to validate which geoelectrical model is more likely to represent the subsurface and at the same time provides a good fit to 1) the surface geology and lithostratigraphic units based on geological cartography of the Baza basin, 2) a qualitative correlation of the models A and B with geological and geophysical constraints, and3) the known Baza fault position and dip angles.

The IGME (Instituto Geologico y Minero de España) has produced 1:50,000 scale geological map of the study area. Based on this cartographic layer, the profile intersects few lithostratigraphic changes at the surface. Starting at the SW, Triassic substrata (basin basement rocks) crop out on the surface. These are covered by Plio-Quaternary glacis levels over Mio-Pliocene fluvio-lacustrine deposits over a short distance along the profile (Fig. 5).

Traces of the Baza Fault are obtained from Quaternary Active Faults Database of Iberia (QAFI). The QAFI database is a joint project between the Spanish Instituto Geológico y Minero de España (IGME) and the Portuguese Laboratório Nacional de Energia e Geologia (LNEG). QAFI provides the most up to date and authoritative inventory of active faults that affect Quaternary rocks and sediments. QAFI aims to capture the main faults displaying tectonic activity in the last 2.6 million years. All faults in the Baza fault zone present a 65° dip angle (Alfaro et al., 2008; Sanz de Galdeano et al., 2012; Haberland et al., 2017).

In addition to the geological information, the Baza Basin has been the subject of numerous geophysical studies to characterize its structure and infilling stratigraphy, including gravimetry and seismic reflection surveys (Figs. 2 and 6). Alfaro et al. (2008) conducted gravity gravity profiling studies covering the Baza Basin. The survey showed an asymmetric negative Bouguer anomaly close to the Baza fault with two gravity minima along the Basin axis running parallel along the fault strike. The Bouguer anomalies were interpreted as variations in the thickness of the basin infill. In the vicinity of DERT survey line, there are two gravimetric survey profile lines, named P2 and P3 in Alfaro et al. (2008) (Fig. 6). The two-dimensional models of the residual gravity anomaly registered on the P2 and P3 profiles provide evidence that the Baza Fault presents a clear half-graben geometry of the hanging wall, with an elongated trough bounded by the normal fault system. Line P-3 intersects the trace of the DERT survey line (Fig. 6) at its north-eastern end. The model used by Alfaro et al. (2008) suggested that at the resolution scale of the gravity data the Baza Fault is a single normal fault located to the East of the topographic range-front boundary, bounding the half graben geometry and with a sedimentary filling thickness of 2400 m.

In 2013, high-resolution seismic profiles were used to image the basin, crossing the Baza Fault in different directions (Haberland et al., 2017). This seismic survey revealed an asymmetric basin shape bounded by Baza Fault, and several other buried faults in the East. Most of these

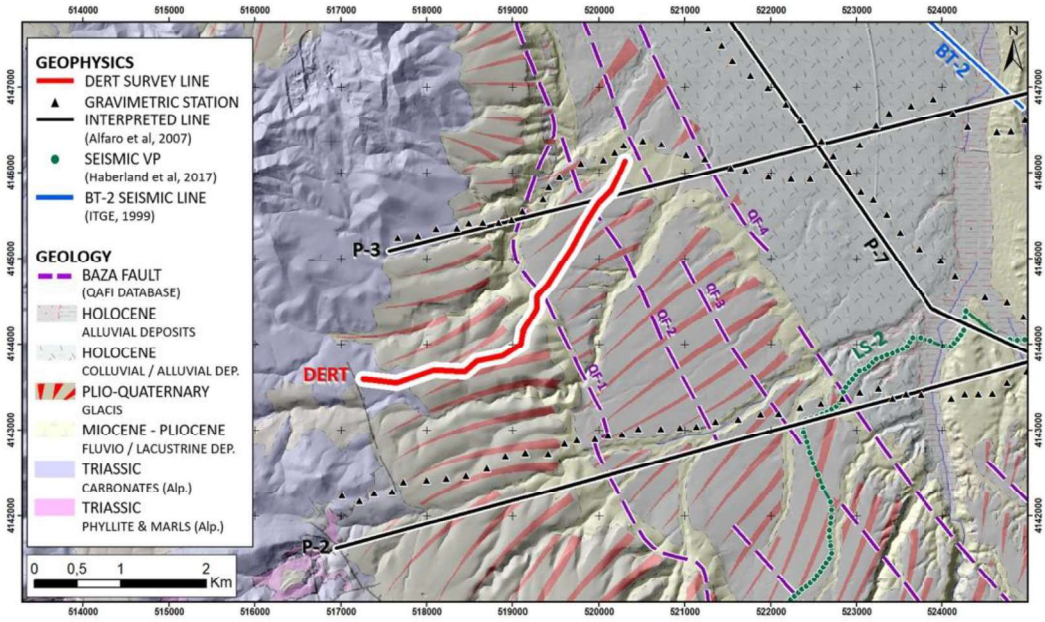

Fig. 6. Geological map of the study area based on 1:50.000 cartography (sheet 994, BAZA, Instituto Geológico y Minero de España (IGME), 1978), with location of the deep electrical resistivity survey line (red), Baza Fault main traces (QAFI database – dashed purple line) and geophysical surveys (black, blue and green dots and lines). (For interpretation of the references to colour in this figure legend, the reader is referred to the web version of this article.)

affect the deeper sedimentary layers of the Baza Basin. The basin was estimated to reach a maximum sediment thickness of 2200 m, in good agreement with the gravity models above (Alfaro et al., 2008). The closest seismic acquisition line to the deep electrical resistivity survey line was LS-2. However, it was still far away from it, so it was not possible to correlate it closely with the electrical resistivity models. Generally, it can only be analyzed in terms of structural style. Due to its long distance and different strike direction from the DERT line, the BT-2 seismic line was also not considered in discussion of the results. Analysis of relevant borehole survey profiles is dealt with in section 5.2.

Model A (Fig. 7-1) shows a good geoelectric correlation with surface outcropping materials, especially in the SW and central part of the model, with the presence of lateral resistivity changes between carbonates, glacis and fluvio-lacustrine materials.

The location and dip angles of two of the identified QAFI faults that were intersected (QF1 and QF2) are compared with the deep electrical resistivity model A. QF1 could be interpreted to continue at depth in the model because the lateral resistivity changes are related to a fault structure discernible in the upper and bottom parts of the model. However, the absence of a sharp resistivity contrast makes it difficult to precisely define its morphology and position. Model A suggests it is a structure with significant lateral displacement with respect to the cartographic position. Fault QF2 is barely identified in A. Weak resistivity with lateral loss of continuity was detected in the upper outcropping resistive sediments of the basin (Plio-Quaternary glacis), and hint at the presence of this fault.

Model A (Fig. 7-1) also correlates well with the IGME surface geology. In the Southwestern part of the model, high resistivity values coincide with the outcropping Triassic carbonate materials. In the central sector, Mio-Pliocene fluvio-lacustrine materials appear as a local resistivity decrease while the higher resistive values in the northeastern part of the model tend to coincide with the Plio-Quaternary glacis.

Although it may appear that the misfit to the data is similar, model B (Fig. 7-2) shows important variations from A, especially considering its correlation with fault information. The resistivity anomalies indicate that the QF1 fault may be located slightly to the West with respect to the QAFI surface trace location. This discrepancy could be due to a locally more complex fault gouge zone or multiple single fault strands like inferred faults 1 and 2 (Fig. 7-2), which cut the Triassic basement to the Northeast. This model shows that the anomalies associated with QF2 are more pronounced, with changes in lateral resistivity due to more resistive infillings among the shallower sediments in the basin. This should be interpreted as a strong indication of a discontinuity. This feature was less evident in model A. Model B correlates better with the outcropping materials, with well-defined lateral resistivity contrasts, especially between the Mio-Pliocene fluvio-lacustrine materials and Plio-Quaternary glacis in the central sector of the model.

5.2. Model interpretation and implications for the Baza fault structure

The electrical resistivity models A and B provide insights into the structure of the fault, in high spatial resolution from the surface down to around 1000 m depth. Both models show good agreement with the general structural geometry of the Baza Basin and a notable correlation with the lithostratigraphic units based on geological cartography. However, model B agrees more accurately with high-spatial resolution and low uncertainty information, such as the mapped surface lithostratigraphic units. Fig. 8 displays a geological interpretation of the preferred model B, including several inferred fault traces, named F1 to F6. Fig. 8 also shows the QAFI database fault positions (QF1 and QF2) and outcropping geological lithostratigraphic units.

The structural interpretation of the preferred model B (Fig. 8-1)

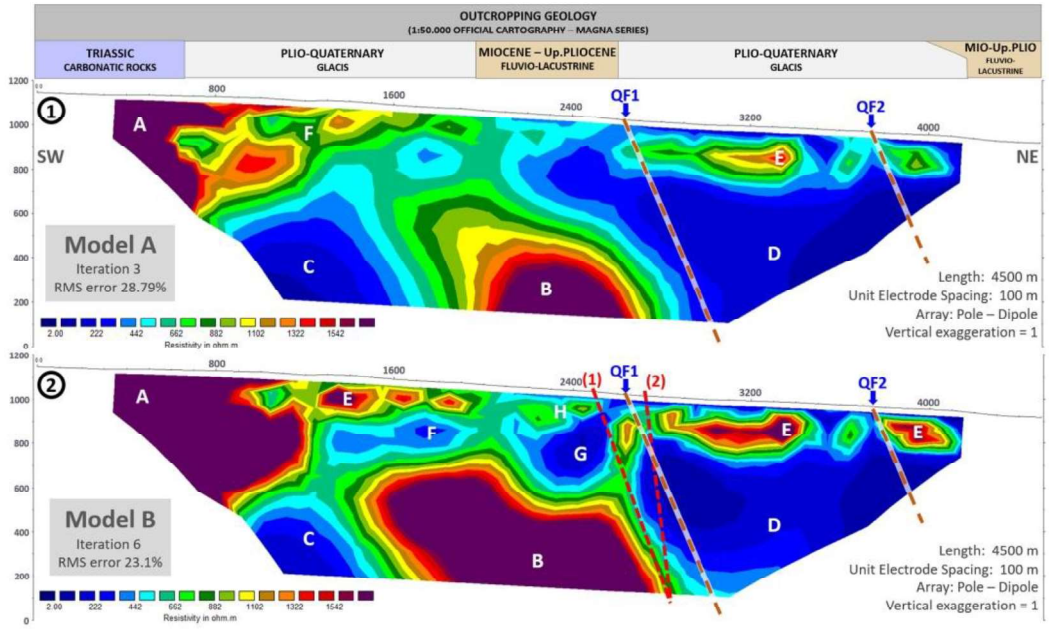

Fig. 7. (1) Model A; (2) Model B. Comparison with available data constraints, namely the outcropping geology (IGME cartography), location and dip angle from known fault traces (QAFI database). The fault plane dip angles were not inferred but taken from the reported 65° in the QAFI database.

shows evidence for up to six faults or structural discontinuities. All structures dip towards the NE, progressively rooting to the basement of the Baza Basin with a staircase morphology. Due to different amounts of inferred normal fault displacement and morphology expression, the faults were interpreted according to two criteria. Fault displacement was estimated using lateral resistivity variations with the assumption they correspond to lithological changes related to the former. This is especially clear in faults involving the variably resistive Triassic materials and conductive basin infillings, and between outcropping glacis levels and fluvio-lacustrine deposits. The first group includes the main inferred faults in terms of size and displacement, named F1, F2 and F3. This set of faults affect the lateral continuity of the resistive Triassic carbonate basement and also the basin infilling materials with a measurable vertical displacement of several hundred metres. The second set of faults, namely F4, F5 and F6, were only inferred by clear loss of lateral continuity of resistivity bodies in the upper infilling basin materials, particularly in the central and northeastern sections of the profile. Consequently, the interpretation of this second set of faults must be taken with caution, as their slip history is not constrained at all, but could provide a useful baseline for further studies.

Fault F1 is located in the western part of the profile and model, close to the 1200 m of the line. According to its morphology, it can be interpreted as a normal fault with a dip angle potentially varying from nearly vertical to 70° to the Northeast. This fault has accumulated a vertical throw, displacing the resistive Triassic basement at ≈ 350 ± 100 m. The fault plane of F1 changes its dip with depth, indicating a potential rotational tilting of the resistive Triassic basement rocks. This could indicate a listric fault geometry (Fig. 8). Based on high-resolution topographic information, the outcropping location coincides with the presence of a minor geomorphological alignment (Fig. 9). Such slope changes, perpendicular to the local drainage system, could be small escarpments compatible with the position and direction of slip along the fault plane. It is suggested that this location should be a target for future additional paleoseismic and/or detailed geological studies, as it affects recent geological deposits and may indicate an active structure.

F2 is also inferred by the rupture and observed vertical displacement of the resistive Triassic basement materials. This fault is clearly visible in the model as a lateral change in resistivity, also affecting the shallow resistive basin-infilling materials. The fault plane presents similar characteristics to F1, displacing the Triassic basement another 250 ± 100 m. The morphology of the basement between F1 and F2, showing a slight apparent dip to the west, indicates block rotation and the listric behavior of these faults. This is also observable in the shallow resistive basin infilling materials between F1 and F2, indicated by a change in the thickness of the materials to the southwest.

These results are novel because to the best of our knowledge the F1 and F2 structures have not been previously identified. The position of these two new faults further west of the topographic range basin front boundary, and the QAFI fault QF1 position, permits displacement of the Baza Basin boundary by ≈ 1300 m to the west (Fig. 9).

Fault F3 is located in the central part of the model, close to the QF1 fault. This fault generated the largest displacement of the Triassic basement materials according to the preferred model B. The fault slip is unbounded but it must be larger than our maximum penetration depth of the DERT method (≈ 1 km). As commented previously, basal Triassic carbonates between F2 and F3 reveal a small apparent dip indicating a potential rotational structure, and suggest a shallow listric fault geometry.

F4, F5 and F6 were interpreted only on the basis of a lateral resistivity change in the upper outcropping resistive fillings of the basin, due to the absence of Triassic basement materials. According to the style observed in the previous faults, a normal-type representation was preferred. F4 seems to be a lesser feature associated with the main fault F3, which generates a local sinking of sedimentary infilling materials in

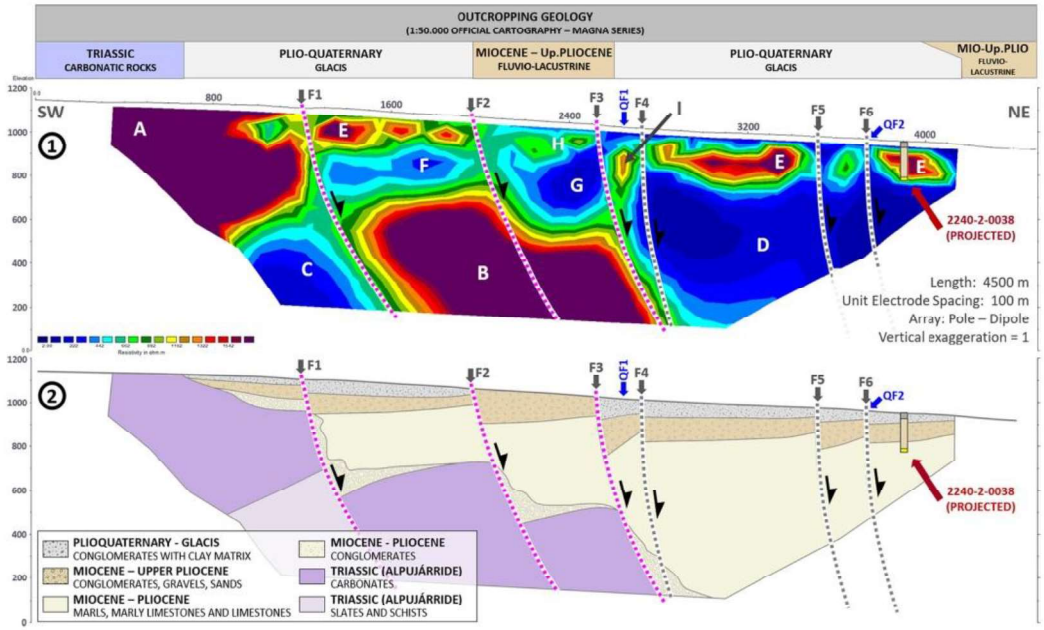

Fig. 8. 1) Structural interpretation of the deep electrical resistivity survey line, including several inferred faults. The F1 to F3 and F4 to F6 fault group were inferred using two different criteria. F1 to F3 are considered main faults, as they affect the Triassic basin basement and its infilling materials, with associated vertical fault displacement. F4 to F6 were inferred due to lateral resistivity changes detectable in the upper infilling basin materials with unknown slip history. QF1 and QF2: QAFI fault position. A to I: geoelectrical bodies discussed in the main text. 2) The preferred litho-stratigraphical interpretative model for the Baza Fault system in this sector, including the projected chrono-stratigraphical interpretation of borehole 2240–2-0038 at the NE end of the line.

the basin (I, Fig. 8-1).

QF2 fault trace intersected Model B in its eastern sector, close to the inferred position for fault F6. The geoelectrical model suggested that if the fault exists it has a small/short displacement history and should only involve materials of similar age and resistive properties. The local lateral resistivity change only affects the upper resistive materials where the F6 fault was interpreted.

In this study, the depth of investigation (DOI) index described by Oldenburg and Li (1999) was determined to assess reliability and to eliminate artefacts produced by mathematical inversion. The DOI index will be close to zero in areas where the final models are constrained well by the data, considering the inversion process to be reliable. However, cells with a DOI index greater than 0.2 were considered less reliable and therefore rejected (Oldenburg and Li, 1999; Thompson et al., 2012; Troiano et al., 2019) (Fig. 10).

This analysis (Fig. 10) shows how the unreliable zones do not affect the interpretation of the preferred geoelectric resistive model (Fig. 8-1 and -2), especially regarding the definition of the inferred fault zones. From the lithological point of view, the preferred resistivity model B shows how the high resistivity Triassic carbonate basement materials (A and B, Fig. 8-1) are strongly affected by the different splays of the Baza Fault. In the westernmost sector of the model, Triassic materials crop out up to the vicinity of F1, being progressively vertically displaced until fault F3, reaching the maximum depth sensitivity of the inversion model (> 1 km depth). Below the resistive Triassic carbonates (ρ > 1500 Ohm•m), a conductive area is discernable (C), probably related to Triassic phyllites, slates and calcschist (C), generating a clear resistivity in contrast with the upper carbonates (García Dueñas et al., 1992; Orozco and Alonso-Chaves, 2002).

In the central and northeastern part of the model and above the high-resistivity Triassic carbonates, conductive materials (ρ < 400 Ohm•m) belonging to the Miocene-Pliocene basin infilling sediments were detected (F, G and D). The resistivity of these materials is variable, but in general more conductive in the central deeper part of the basin (NE). The transition between resistive Triassic carbonates and conductive infillings is often gradual, indicating the presence of proximal breccias and conglomerates. These proximal sediments are especially noticeable close to the main faults, in concordance with deposition models of the basin.

More resistive materials (ρ > 400 Ohm•m) can be found in the shallower part of the profile (less than 300 m depth), which is associated with a higher granulometry of Miocene - upper Pliocene materials (E and H). These materials present lateral changes in resistivity that may be linked to fault discontinuities or local compositional rock variations. Glacis deposits are rarely observed in the profile because of their outcropping position and thickness. According to the cartographic data, glacis may have a maximum thickness of ≈50 m, coinciding with the loss of resolution of our model at shallow depths due to our minimum electrode spacing (≈100 m).

Fig. 8-2 shows a tectonic and litho-stratigraphic interpretation of our preferred geoelectrical model. According to this interpretation, the Baza Fault system could be a complex structure more than 2 km wide, with at least three and possibly six normal fault branches and a listric geometry. These faults affect the basin basement and infillings, indicating a long history of normal faulting displacement. The fault system generates an asymmetric segmentation with increasing basin thickness to the SW, clearly observable in the upper Miocene to Plio-Quaternary units. The results confirm that the fault should be active as present-day tectonic

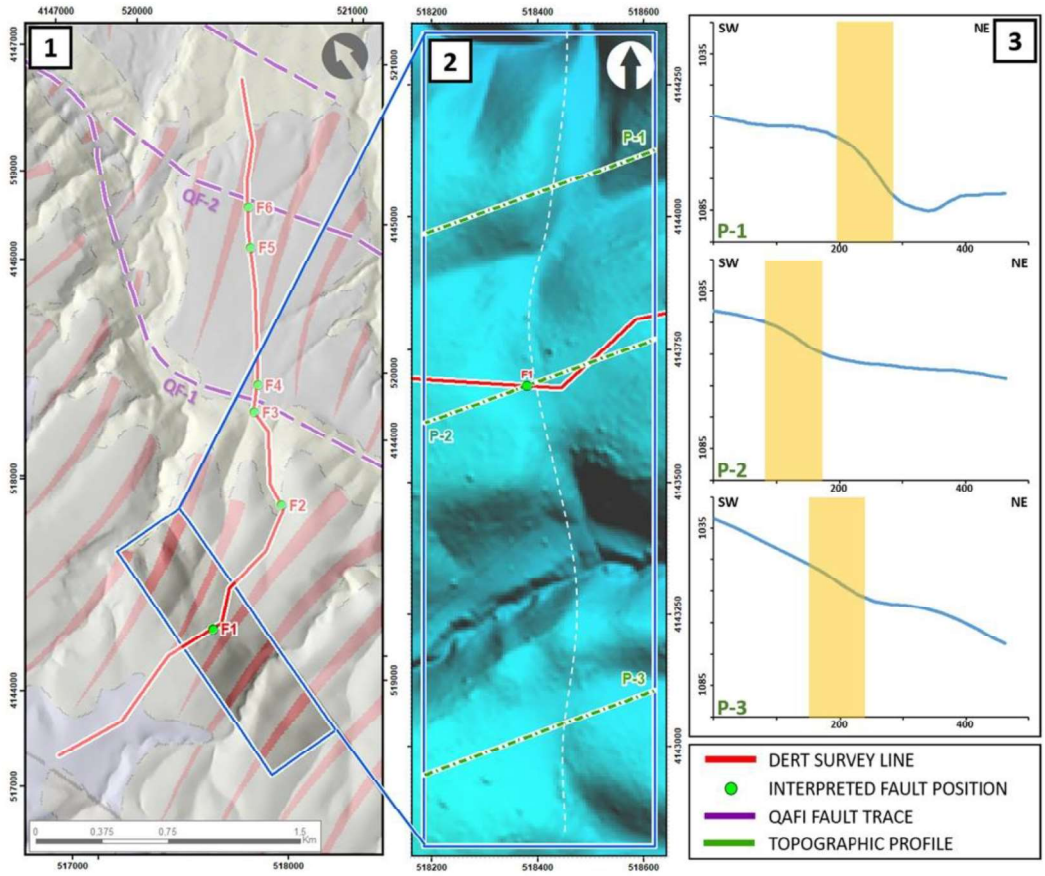

Fig. 9. Topographic analysis of fault F1. 1) Deep electrical resistivity survey line position, with inferred fault positions (F1 to F6), QAFI fault traces and topographic analysis area (blue rectangle). 2) Hillshade representation of the analysis area topography showing position of the interpreted F1 fault, deep electrical resistivity survey line, and topography analysis profiles (P-1 to P-3). The white dashed line represents a potential alineation of the F1 fault. 3) Topographic analysis profiles P-1, P-2 and P-3 showing escarpments (orange areas) compatible with a fault. (For interpretation of the references to colour in this figure legend, the reader is referred to the web version of this article.)

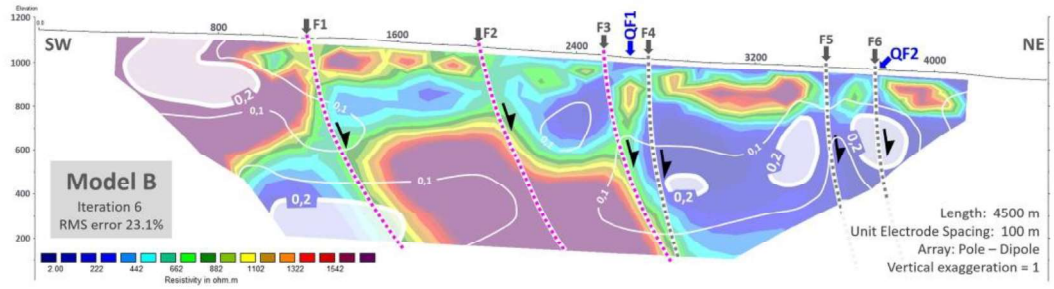

Fig. 10. Depth of Investigation Index (DOI) of the resistivity model. Cells with DOI index greater than 0.2 are considered less reliable. This figure shows how the obtained DOIN index do not affect the structural interpretation of the model (Fig. 8).

faults due to the fact that they are cutting through all the sedimentary materials, including glacis Plio-Quaternary levels. This is particularly the case of the previously unrecognized fault F1, which has geomorphic expression (5–10 m) (Fig. 11).

In this study, public databases of boreholes (lithologic or geophysical core drilling) in the vicinity of the line of investigation were consulted for better interpretation. According to the lithological scheme available, the 2240–2-0038 code borehole reached a depth of 185 m. The column shows a complex lithological succession with alternation of conglomerates, sands, marls, silts and clays. Unfortunately, there are no chronostratigraphic differentiations in the public database. Moreover, a tentative analysis of that column suggests an increase in clay content from 141 to 173 m, which could be interpreted as a change in sedimentation regime. This change may reflect a different age, possibly the transition between Plio-Quaternary and upper Mio-Pliocene materials to lower Mio-Pliocene materials, with a mainly marly character (Fig. 12-2). However, a precise interpretation was not possible without further geological analysis.

Borehole 2240–2-0038 can be projected at around 3800–4000 m of the profile, taking into account the structure of the study area and position of the main faults. The interpretation of the borehole was analyzed by the geoelectric resistive model and its geological interpretation (Figs. 8-1 and -2). Overall, a correspondence was observed between the borehole geology and the geoelectric model (Fig. 8), but there were significant divergences in the thickness of the stratigraphic layers. These differences are to be expected, owing to the uncertainty of the borehole location with respect to the profile and spatial resolution of the inverted model.

6. Conclusions

This study presents the new results of a deep electrical resistivity tomography (DERT) study to gain insights into the shallow geometry of the Baza Fault system. The DERT model is sensitive to structures with depth ranges complementary to previous gravity and seismic and surface geology. Specifically, this investigation was conducted in the southwestern part of the Baza Basin. Resistivity data were obtained using two 3 km long multicore reversible cables with electrode spacing of 100 m to allow a depth penetration of more than 1 km. The inversion models are in good agreement with geological and geophysical constraints. The preferred resistivity model presents resistivity values ranging from 20 to 3000 Ohm•m, which were calibrated with the lithostratigraphic characteristics and fault database position (QAFI). A new, more detailed geological and structural view of the Baza Fault is provided.

The results strongly support that the main strand of the system is the fault here named F3, close to the known QF1 mapped in the QAFI database. This F3/QF1 structure progressively plunges the Triassic basement below the maximum penetration depth of the DERT method (indicating a cumulative slip history of >1 km). The new model furnishes higher-spatial resolution information at depth for the Baza fault system, and supports a segmented active normal fault system, considerably wider than previously recognized (> 2 km wide). This study confirms that, as in previous studies, the Baza fault system consist of northeast dipping normal faults controlling the basin's development and structure. The inferred structures suggest progressive change in dip angle with depth, supporting listric fault geometries.

A fault system located southwestward of QF1 emerges with this study. A previously unmapped fault (F1) with significant accumulated slip, located west from previous known faults and hence representing a major basin-bounding fault (1300 m southwestward of QF1) was determined. F2 is another unmapped fault located between (F1) and (QF1), inferred by the rupture and observed vertical displacement of the resistive Triassic basement materials. In addition, there is geophysical, and possible geomorphic, evidence suggesting that F1 is an active fault affecting the youngest Plio-Quaternary glacis levels. It is expected that these new results will motivate future paleoseismologic studies on this candidate fault(s).

Our study has revealed that the deep electrical resistivity research method can be an important tool to study active fault systems, such as Baza. It is thought that the method applied in this study will be a complementary method in regional gravity and seismic surveys and detailed geological mapping. The results from deep electrical resistivity models can improve the identification of seismogenic active faults.

Authors statement

We, the authors, declare that this material is new and has not been

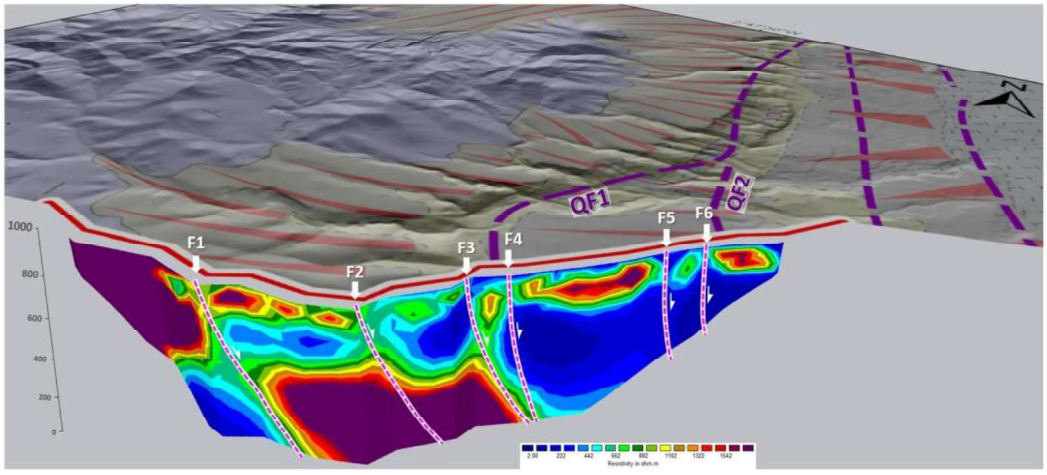

Fig. 11. 3D sketch showing the fault interpretation along the deep electrical resistivity tomography (DERT) survey line with geological cartography and fault traces according to the Quaternary Active Faults Database of Iberia (QAFI). The presence of new faults F1 and F2, and conductive infilling materials, shows a western position of the Baza Basin limit.

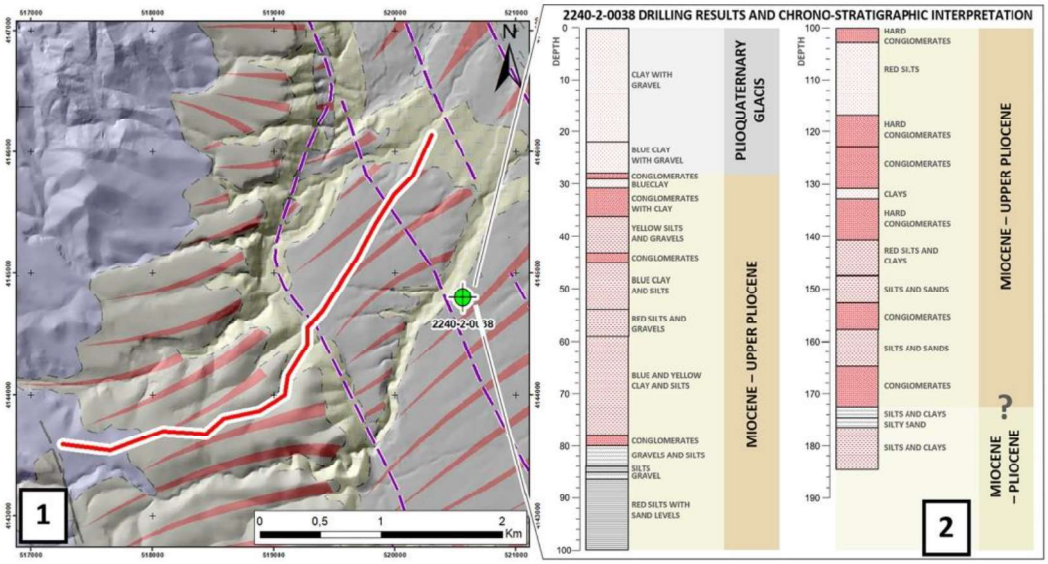

Fig. 12. 1) Geological map of the study area based on 1:50.000 cartography (sheet 994, BAZA, Instituto Geológico y Minero de España (IGME), 1978), with location of the deep electrical resistivity (DERT) survey line (red), Baza Fault main fault traces (QAFI database – dashed purple line), geophysical surveys (black, blue and green dots and lines), and boreholes with lithological information (Instituto Geológico y Minero de España, Base de datos de puntos de agua (http://info.igme.es/BDAguas/), SIGEOF, Sistema de informacion Geofísica (http://info.igme.es/sigeof/) and Litoteca de sondeos (http://www.igme.es/servicios/litoteca.htm)). 2) Lithological scheme of borehole 2240–2-0038, located 950 m to the SE of the survey line, and a tentative chrono-stratigraphic interpretation. (For interpretation of the references to colour in this figure legend, the reader is referred to the web version of this article.)

submitted to any other journal.

Declaration of Competing Interest

We, the authors, declare that we do not have any conflict of interest regarding the content of the manuscript submitted to Journal of Applied Geophysics.

Acknowledgments

The project was funded by GEOLAND SERVICES SL and Técnicas Geofísicas SL. The authors appreciate the assistance of anonymous reviewers for their comments and support on this paper, especially professor D. Pedro Carrasco Morillo. Without his vision this work would not have been possible. This manuscript has been edited by Guido Jones, currently funded by the Cabildo de Tenerife, under the TFinnova Programme supported by MEDI and FDCAN funds. PJG's contribution was supported by the Spanish Ministerio de Ciencia e Innovación research project COMPACT (proyecto PID2019-104571RA-I00 de investigación financiado por MCIN/AEI/10.13039/501100011033) and a 2020 Leonardo Fellowship Grant for Researchers and Cultural Creators, BBVA Foundation (IN[20]_CMA_CCT_0015).

References

Alfaro, P., Moretti, M., Soria, J.M., 1997. Soft-sediment deformation structures induced by earthquakes (seismites) in Pliocenelacustrine deposits (Guadix-Baza Basin, Central Betic Cordillera). Eclogae Geol. Helv. 90, 531–540. https://doi.org/10.5169/seals-168193.

Alfaro, P., Delgado, J., Sanz de Galdeano, C., Galindo Zaldívar, J., García-Tortosa, F.J., López-Garrido, A.C., López-Casado, C., Marín-Lechado, A., Gil, A., Borque, M.J., 2008. The Baza Fault: a major active extensional fault in the central Betic Cordillera (south Spain). Int. J. Earth Sci. 97, 1353–1365. https://doi.org/10.1007/s00531-007-0213-z.

Balasco, M., Galli, P., Giocoli, A., Gueguen, E., Lapenna, V., Perrone, A., Iscitelli, S.P., Rizzo, E., Romano, G., Siniscalchi, A., Votta, M., 2011. Deep geophysical electromagnetic section across the middle Aterno Valley (Central Italy): preliminary results after the April 6, 2009 L'Aquila earthquake. Boll. Geofis. Teor. Appl. 52 (3). 443–455. https://doi.org/10.4430/bgta0028.

Biasi, G., Wesnousky, S., 2017. Bends and ends of surface ruptures. Bull. Seismol. Soc. Am. 107, 2543–2560. https://doi.org/10.1785/0120160292.

Caputo, R., Piscitelli, S., Oliveto, A., Rizzo, E., Lapenna, V., 2003. High-resolution resistivity tomographies in active tectonic studies. Examples from the Tyrnavos Basin, Greece. J. Geod. 36 (1–2), 19–35. https://doi.org/10.1016/S0264-3707(03)00036-X.

Carrasco García, P., 2013. Avance en Técnicas Geofísicas para la caracterización del subsuelo mediante innovación y el uso de herramientas de gestión de información espacial. PhD Thesis. Escuela Politécnica Superior de Avila. Univ de Salamanca, 523 pp.

Carrier, A., Fischanger, F., Gance, J., Cocchiararo, G., Morelli, G., Lupi, M., 2019. Deep electrical resistivity tomography for the prospection of low-to medium enthalpy geothermal resources. Geophys. J. Int. 219, 2056–2072. https://doi.org/10.1093/gji/ggz411.

Castro, J., Martin-Rojas, I., Medina-Cascales, I., García-Tortosa, F.J., Alfaro, P., Insua-Arévalo, J.M., 2018. Active faulting in the central Betic Cordillera (Spain): palaeoseismological constraint of the surface-rupturing history of the Baza Fault (Central Betic Cordillera, Iberian Peninsula). Tectonophysics 736, 15–30. https://doi.org/10.1016/j.tecto.2018.04.010.

Drahor, M.G., Berge, M.A., 2017. Integrated Geophysical Investigations in A Fault Zone located on Southwestern part of Izmir City, Western Anatolia, Turkey. J. Appl. Geophys. 136, 114–133. https://doi.org/10.1016/j.jappgeo.2016.10.021.

Edwards, L.S., 1977. A modified pseudosection for resistivity and IP. Geophysics 42, 1020–1036. https://doi.org/10.1190/1.1440762.

Galindo Zaldívar, J., González-Lodeiro, F., Jabaloy, A., 1989. Progressive extensional shear structures in a detachment contact in the Western Sierra Nevada (Betic Cordilleras, Spain). Geodin. Acta 3 (1), 73–85. https://doi.org/10.1080/09853111.1989.11105175.

Galindo Zaldívar, J., Jabaloy, A., Serrano, I., Morales, J., González- Lodeiro, F., Torcal, F., 1999. Recent and present-day stresses in the Granada Basin (Betic Cordilleras): example of a late Miocene-present-day extensional basin in a convergent plate boundary. Tectonics 18 (4), 686–702. https://doi.org/10.1029/1999TC900016.

García Tortosa, F.J., Alfaro, P., Galindo Zaldívar, J., Gibert, L., López Garrido, A.C., Sanz de Galdeano, C., Ureña, M., 2008. Geomorphologic evidence of the active Baza Fault

(Betic Cordillera, South Spain). Geomorphology 97 (3–4), 374–391. https://doi.org/10.1016/j.geomorph.2007.08.007.
García Tortosa, F.J., Alfaro, P., Galindo Zaldívar, J., Sanz de Galdeano, C., 2011. Glacis geometry as a geomorphic marker of recent tectonics: the Guadix-Baza Basin (South Spain). Geomorphology 125 (4), 517–529. https://doi.org/10.1016/j.geomorph.2010.10.021.
García-Dueñas, V., Balanyá, J.C., Martínez-Martínez, J.M., 1992. Miocene extensional detachments in the outcropping basement of the northern Alboran Basin (Betics) and their tectonic implications. Geo-Marine Lett. 12, 88–95. https://doi.org/10.1007/BF02084917.
García-Dueñas, V., Banda, E., Torné, M., Cordoba, D., ESCI-Béticas Working Group, 1994. A deep seismic reflection survey across the Betic Chain (Southern Spain): first results. Tectonophysics 232, 77–89. https://doi.org/10.1016/0040-1951(94)90077-9.
García-García, F., Fernández, J., Viseras, C., Soria, J.M., 2006. Architecture and sedimentary facies evolution in a delta stack controlled by fault growth (Betic Cordillera, southern Spain, late Tortonian). Sediment. Geol. 185 (1–2), 79–92. https://doi.org/10.1016/j.sedgeo.2005.10.010.
Gibert, L., Sanz de Galdeano, C., Alfaro, P., López Garrido, A.C., 2005. Seismic-induced slump in early Pleistocene deltaic deposits of the Baza Basin (SE Spain). Sediment. Geol. 179 (3), 279–294. https://doi.org/10.1016/j.sedgeo.2005.06.003.
Günther, Thomas, Schaumann, Gerlinde, Musmann, Patrick, Grinat, Michael, 2011. Imaging of a Fault Zone by a Large-scale DC Resistivity Experiment and Seismic Structural Information. https://doi.org/10.3997/2214-4609.20144450.
Haberland, C., Giber, L., Jurado, M.J., Stiller, M., Baumann- Wilke, M., Scott, G., Mertz, D.F., 2017. Architecture and tectono-stratigraphic evolution of the intramontane Baza Basin (Betics, SE-Spain): constraints from seismic imaging. Tectonophysics 709, 69–84. https://doi.org/10.1016/j.tecto.2017.03.022.
IGN (Spanish Instituto Geográfico nacional) seismic Catalogue, 2020. https://www.ign.es/web/sis-catalogo-terremotos.
Instituto Geológico y Minero de España (IGME), 1978. Mapa geológico de la hoja nº 994 (Baza Hoja de Baza 994). Mapa Geológico de España E. 1:50.000. Segunda Serie (MAGNA), Primera edición. IGME. Depósito legal: M-6791-1978.
Jabaloy, A., Galindo Zaldivar, J., Gonzalez-Lodeiro, F., Aldaya, F., 1995. Main features of the deep structure of the central Betic Cordillera (SE Spain) from the ESCI-Béticas deep seismic reflection profiles. Rev. Soc. Geol. Esp. 8 (4), 461–476.
Kolawole, F., Atekwana, E.A., Laó-Dávila, D.A., Abdelsalam, M.G., Chindandali, P.R., Salima, J., Kalindekafe, L., 2018. High-resolution electrical resistivity and aeromagnetic imaging reveal the causative fault of the 2009 M_w 6.0 Karonga, Malawi earthquake. Geophys. J. Int. 213 (2), 1412–1425. https://doi.org/10.1093/gji/ggy066.
Lines, L.R., Treitel, S., 1984. Tutorial: a review of least-squares inversion and its application to geophysical problems. Geophys. Prospect. 32, 159–186. https://doi.org/10.1111/j.1365-2478.1984.tb00726.x.
Loke, M.H., 2019. Rapid 2-D Resistivity and IP inversión Using the Least-Squares Method. Geotomo Software, Malaysia, 146 pp.
Loke, M.H., Barker, R.D., 1995. Least square inversion of apparent resistivity pseudosections. Geophysics 60, 1682–1690. https://doi.org/10.1190/1.1443900.
Loke, M., Dahlin, T., 2002. A comparison of the Gauss–Newton and quasi-Newton methods in resistivity imaging inversion. J. Appl. Geophys. 49 (3), 149–162. https://doi.org/10.1016/S0926-9851(01)00106-9.
Marín-Lechado, C., Pedrera, A., Peláez, J.A., Ruiz-Constán, A., González-Ramón, A., Henares, J., 2017. Deformation style and controlling geodynamic processes at the eastern Guadalquivir foreland basin (Southern Spain). Tectonics 36, 1072–1089. https://doi.org/10.1002/2017TC004556.
Martínez-Solares, J.M., Mezcua, J., 2002. Catálogo sísmico de la Península Ibérica (800 AC-1900). Madrid (Spain), Instituto Geográfico Nacional (IGN). Monografía 18, 254 pp.
Medina-Cascales, I., Martin-Rojas, I., García-Tortosa, F.J., Peláez, J.A., Alfaro, P., 2020. Geometry and kinematics of the Baza Fault (central Betic Cordillera, South Spain): insights into its seismic potential. Geol. Acta 18 (11), 1–25. https://doi.org/10.1344/GeologicaActa2020.18.11.
Nocquet, J.-M., 2012. Present-day kinematics of the Mediterranean: A comprehensive overview of GPS results. Tectonophysics 579, 220–242. https://doi.org/10.1016/j.tecto.2012.03.037.
Oldenburg, D.W., Li, Y., 1999. Estimating depth of investigation in DC resistivity and IP surveys. Geophysics 64, 403–416. https://doi.org/10.1190/1.1444545.
Orozco, M., Alonso-Chaves, F.M., 2002. Estructuras de colapso extensional en el Dominio de Alborán. In: Orozco, M. (Ed.), Región de La Axarquía-Sierra Tejeda (provincias de Málaga y Granada). XIV Reunión de la Comisión de Tectónica de la Sociedad Geológica de España, Guía de Campo, Granada, 120pp. ISBN: 84-607-5712-9.
Pace, B., Visini, F., Peruzza, L., 2016. FiSH: MATLAB tools to turn fault data into Seismic-Hazard Models. Seismol. Res. Lett. 87 (2A), 374–386. https://doi.org/10.1785/0220150189.
Palano, M., González, P.J., Fernández, J., 2013. Strain and stress fields along the Gibraltar Orogenic Arc: Constraints on active geodynamics. Gondwana Res. 23 (3), 1071–1088. https://doi.org/10.1016/j.gr.2012.05.021.
Palano, M., González, P.J., Fernández, J., 2015. The Diffuse Plate boundary of Nubia and Iberia in the Western Mediterranean: Crustal deformation evidence for viscous coupling and fragmented lithosphere. Earth Planet. Sci. Lett. 430, 439–447. https://doi.org/10.1016/j.epsl.2015.08.040.
Pérez-Peña, J.V., Azañón, J.M., Galve, J.P., Booth-Rea, G., de Lis Mancilla, F., Stich, D., Morales, J., 2018. A post-Tortonian pull-apart basin controlled by lithosphere tearing processes at a STEP boundary of the Gibraltar Arc Subduction System. In: 20th EGU General Assembly, EGU2018, Proceedings from the Conference held 4-13 April, 2018 in Vienna, Austria, p. 15695. https://ui.adsabs.harvard.edu/abs/2018EGUGA..2015695P/abstract.
Pucci, S., Finizola, S., Civico, R., Sapia, V., Barde-Cabusson, S., Orefice, S., Peltier, A., Villani, F., Ricci, T., De Martini, P.M., Brothelande, E., Poret, M., Gusset, R., Torres, L., Delcher, E., Daniela, Pantosti, Mezon, C., Suski, B., 2016. Deep electrical resistivity tomography along the tectonically active Middle Aterno Valley (2009 L'Aquila earthquake area, Central Italy). Geophys. J. Int. 207 (2), 967–982. https://doi.org/10.1093/gji/ggw308.
Rizzo, E., Giamapolo, V., 2019. New deep electrical resistivity tomography in the High Agri Valley basin (Basilicata, Southern Italy). Geomat. Nat. Hazards Risk 10 (1), 197–218. https://doi.org/10.1080/19475705.2018.1520150.
Rizzo, E., Colella, A., Lapenna, V., Piscitelli, S., 2004. High-resolution images of the fault-controlled High Agri Valley basin (Southern Italy) with deep and shallow electrical resistivity tomographies. Phys. Chem. Earth 29, 321–327. https://doi.org/10.1016/j.pce.2003.12.002.
Rizzo, E., Giampaolo, V., Capozzoli, L., Grimaldi, S., 2019. Deep Electrical Resistivity Tomography for the Hydrogeological setting of Muro Lucano Mounts Aquifer (Basilicata, Southern Italy). Geofluids 2019, 6594983. https://doi.org/10.1155/2019/6594983.
Robain, H., Bobachev, A., 2002. X2IPI Tool Box for 2D DCand DC-IP Measurements. http://geophys.geol.msu.ru/x2ipi/x2ipi.html#boba.
Rodríguez-Fernandez, J., Azor, A., Azañón, J., 2012. The betic intramontane basins (SE Spain): stratigraphy, subsidence, and tectonic history. In: Tectonics of Sedimentary Basins, pp. 461–479. https://doi.org/10.1002/9781444347166.ch23.
Sanz de Galdeano, C., Vera, J.A., 1992. Stratigraphic record and palaeogeographical context of the Neogene basins in the Betic Cordillera, Spain. Basin Res. 4 (1), 21–36. https://doi.org/10.1111/j.1365-2117.1992.tb00040.x.
Sanz de Galdeano, C., Vera, J.A., 2007. Stratigraphic record and palaeogeographical context of the Neogene basins in the Betic Cordillera, Spain. Basin Res. 4, 21–36. https://doi.org/10.1111/j.1365-2117.1992.tb00040.x.
Sanz de Galdeano, C., García-Tortosa, F.J., Peláez, J.A., Alfaro, P., Azañón, J.M., Galindo Zaldívar, J., López-Casado, C., López- Garrido, A.C., Rodríguez-Fernández, J., Ruano, P., 2012. Main active faults in the Granada and Guadix-Baza Basins (Betic Cordillera). J. Iber. Geol. 38 (1), 209–223. https://doi.org/10.5209/rev_JIGE.2012.v38.n1.39215.
Sanz de Galdeano, C., Azañón, J.M., Cabral, J., Ruano, P., Alfaro, P., Canora, C., Ferrater, M., García-Tortosa, F., Mayordomo, J., Gràcia, E., Insua-Arévalo, J.M., Jiménez, A., Lacan, P., Marín-Lechado, C., Martín-Banda, R., Martín-González, F., Martínez-Díaz, J.J., Martín-Rojas, I., Masana, E., Simón, J.L., 2020. Active faults in Iberia. In: Quesada, C., Oliveira, J. (Eds.), The Geology of Iberia: A Geodynamic Approach. Springer. Cham. Regional Geology Reviews. pp. 33–75.
Scholz, C.H., 2019. The Mechanics of Earthquakes and Faulting, 3rd edition. Cambridge University Press, Cambridge. 493pp.
Soria, J.M., Viseras, C., Fernandez, J., 1998. Late Miocene–Pleistocene tectono-sedimentary evolution and subsidence history of the central Betic Cordillera (Spain): A case study in the Guadix intramontane basin. Geol. Mag. 135 (4), 565–574. https://doi.org/10.1017/S0016756898001186.
Steeples, D.W., 2001. Engineering and environmental geophysics at the millenium. Geophysics. 66 (1), 31–35. https://doi.org/10.1190/1.1444910.
Storz, H., Storz, W., Jacobs, F., 2000. Electrical resistivity tomography to investigate geological structures of the earth's upper crust. Geophys. Prospect. 48, 455–471. https://doi.org/10.1046/j.1365-2478.2000.00196.x.
Suzuki, K., Toda, S., Kusunoki, K., Fujimitsu, Y., Mogi, T., Jomori, A., 2000. Case studies of electrical and electromagnetic methods applied to mapping active faults beneath the thick quaternary. Dev. Geotech. Eng. 84, 29–45. https://doi.org/10.1016/S0165-1250(00)80005-X.
Telford, W.M., Geldart, L.P., Sheriff, R.E., 1990. Applied Geophysics, 2nd ed. Cambridge Univ. Press, Cambridge, UK. https://doi.org/10.1017/CBO9781139167932.
Thompson, S., Kulssa, B., Luckman, A., 2012. Integrated electrical resistivity tomography (ERT) and self-potential (SP) techniques for assessing hydrological processes within glacial lake moraine dams. J. Glaciol. 58 (211), 849–858. https://doi.org/10.3189/2012JoG11J235.
Troiano, A., Isaia, R., Di Giuseppe, M.G., Tramparulo, D.A., Vitale, S., 2019. Deep electrical resistivity tomography for a 3D picture of the most active sector of Campi Flegrei caldera. Sci. Rep. 9, 15124. https://doi.org/10.1038/s41598-019-51568-0.
Vera, J.A., 1970a. Facies del Plioceno de la Depresión de Guadix- Baza. Cuadernos Geol. Univ. Granada 1, 23–25.
Vera, J.A., 1970b. Estudio estratigráfico de la Depresión de Guadix-Baza. Boletín Inst. Geol. Miner. Esp. 81, 429–462.
Wells, D.L., Coppersmith, K.J., 1994. New empirical relationships among magnitude, rupture length, rupture width, rupture area, and surface displacement. Bull. Seismol. Soc. Am. 84 (4), 974–1002. https://doi.org/10.1785/BSSA0840040974.
Wesnousky, S.G., 2008. Displacement and geometrical characteristics of earthquake surface ruptures: issues and implications for seismic-hazard analysis and the process of earthquake rupture. Bull. Seismol. Soc. Am. 98 (4), 1609 1632. https://doi.org/10.1785/0120070111.